ON THE COMPARISON OF STALLING FLOW-THROUGH NACELLES AND POWERED INLETS AT TAKE-OFF CONDITIONS

S. Schulze, C. Kähler, R. Radespiel
Institute of Fluid Mechanics, TU Braunschweig
Bienroder Weg 3, 38106 Braunschweig
Germany

OVERVIEW

Numerical 3D simulations with a RANS flow solver are conducted to investigate the separation behaviour of a powered inlet at take-off conditions. At the limit of the flight envelope the simulation of powered engines still needs major improvement and therefore a novel simulation methodology has to be developed. This paper prepares for the necessary validation experiments on a flow-through nacelle in a low-speed wind tunnel. Because of the high costs of air intake venting devices basic wind tunnel experiments arrange rather for a flow-through nacelle than an engine with an integrated fan and a realistic mass flow rate. The objective is therefore to design and analyse a flow-through nacelle with a boundary layer loading similar to powered engines.
The typical separation on the intake inner bottom lip of powered inlets during take-off is numerically investigated for a reference nacelle, and the simulations are compared to the relating measured data. Based on the results of this analysis a design methodology for the flow-through nacelle is established and successfully applied. During the design process a variety of parameters is analysed to control separation onset.

1. NOMENCLATURE

Ma	Mach number
Re	Reynolds number
c	chord length
$c_{f,x}$	wall shear stress coefficient in the direction of the oncoming flow
c_p	pressure coefficient
f	camber
$\dot{m}$	mass flow rate
x,y,z	Cartesian coordinates
α	angle of attack
φ	diffuser angle
θ	angle defining a circumferential section of a nacelle
θ_{rel}	angle of separation bubble spread in circumferential direction
DFG	Deutsche Forschungsgemeinschaft
DLR	Deutsches Zentrum fuer Luft- und Raumfahrt
MUB	Modell-Unterschallwindkanal Braunschweig
PIV	Particle Image Velocimetry
RANS	Reynolds-averaged Navier-Stokes
SA	Spalart Allmaras
SAE	Spalart Allmaras, Edwards Modification

2. INTRODUCTION

The aerodynamic separation behaviour with large separated flow regions is hard to seize in experiments as well as in numerical simulations. Large scale separations are usually unsteady and often feature the phenomena of vortex shedding. Regarding engine inlets of transport aircrafts separation leads to a non-uniform and unsteady onstream to the fan stage. Fluctuations in mass flow and pressure distribution as well as the angular momentum in the inlet can give rise to separation at the compressor sections and to strong dynamic loadings on the blades (flutter) which in turn causes the engine to run instable.
While numerical simulation methods for the flight design point are well developed, the simulation of powered engines at the limit of the flight envelope needs major improvement. In order to enable the development of sophisticated simulation methodologies, wind tunnel experiments are essential for validation purposes. For engines experimental data regarding the size and dynamics of the vortex structures as well as the hysteresis behaviour at separation is of great interest. The prospective numerical simulation methodologies need experimental evidence at what flow states the scales of the unsteady vortex shedding can be separated from the scales of the turbulent fluctuations. In order to answer this question the convection velocity of the vortex structures has to be determined in dependency on their size and their distance normal to the wall.
In the past the separation behaviour of engine inlets with angle of attack was investigated with conventional probe measurement techniques. The state of the art can be extracted from the publications of special symposia [1],[2] and can also be found in the literature concerning engine design [3]. Systematic investigations of geometry influences on the separation behaviour of engines were published in [4]. In more recent research the inlets of transport aircrafts were analysed with pitot tubes which featured partially time-resolved measurement techniques[5]. Thus conclusions to the unsteady flow field are confined and it can be stated that no systematic results regarding the unsteady flow structures in the inlets of

transport aircrafts are known which are sufficient for the planned validation of the improved simulation methodology.
The identification and statistic characterization of the spatial vortex structures is planned to be carried out with non-intrusive velocity field measurement techniques because the formation and the dynamics of the uniform moving structures is not subject to deterministic conditions. In recent years there was great progress in the development of different kinds of Particle Image Velocimetry, e.g. high-resolution stereo [6], microscopic [7],[8], tomographic [9],[10] and time-resolved [11] flow field measurements, making detailed flow analysis possible.

3. LARA NACELLE

As a reference for a powered engine inlet at take-off the separation behaviour of the so-called LARA nacelle (see. FIG. 1) is numerically analysed. The nacelle was designed as part of the Laminar Flow Research Action programme in the early nineties [12] and was analysed in the pressurized ONERA F1 wind tunnel.

3.1. Numerical Flow Simulation

The numerical solutions of the Reynolds-averaged Navier-Stokes equations are computed using the DLR hybrid unstructured flow solver TAU [13]. The code is based on a finite-volume scheme and combines the advantages of structured grids to resolve the boundary layer with the flexible grid generation of unstructured grids (see FIG. 1). To accelerate the convergence to steady state techniques like local time stepping, residual smoothing and multi-grid are available. Present simulations were performed assuming a fully turbulent boundary layer after no differences could be found in the results of computations with and without a pre-defined transition. As a turbulence model “Menter SST” [14] was selected.
The unstructured hybrid grids were generated using the commercial code Gridgen [15], and the total number of points is about 600,000 for all LARA simulations. To resolve the boundary layer 54 layers with prismatic hexaeders were introduced.

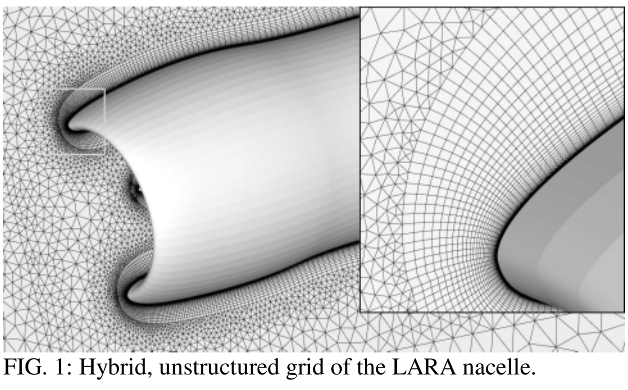

FIG. 1: Hybrid, unstructured grid of the LARA nacelle.

3.2. Results of 3D Simulations

For the 3D simulations Mach number, Reynolds number and mass flow rate should represent real take-off conditions. On the other hand these parameters had to match a measurement series of the ONERA wind tunnel experiments[16]. Thus the computations were undertaken at $Ma = 0.25$, $Re = 11.2\times10^6$, and a mass flow rate of $\dot{m} = 1264\,\mathrm{kg/s}$ was considered which is close to the inlet mass flow of a Trent 900 engine at take-off conditions.
The LARA nacelle was found to separate at the intake inner bottom lip ($\theta = 180°$) at $\alpha = 17.5°$ in accordance to the above mentioned literature. FIG. 2 shows the flow field of the LARA nacelle immediately after the separation onset at $\alpha = 18.0°$.

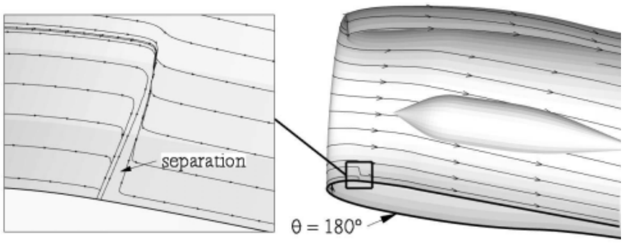

FIG. 2: Flow field of the LARA nacelle at $Ma = 0.25$, $Re = 11.2\times10^6$, $\dot{m} = 1264\,\mathrm{kg/s}$, $\alpha = 18.0°$.

The narrow turbulent separation bubble in FIG. 2 indicates that the LARA nacelle features a shock-induced separation due to a supersonic region in the inlet around $\theta = 180°$. Since it is not possible to produce a shock-induced separation in a flow-through nacelle at low-speed wind tunnel conditions, the mass flow rate was varied in order to produce a range of characteristic pressure distributions. FIG. 3 and 4 show the pressure and shear stress distributions for mass flow rates down to 900 kg/s right before separation onset.

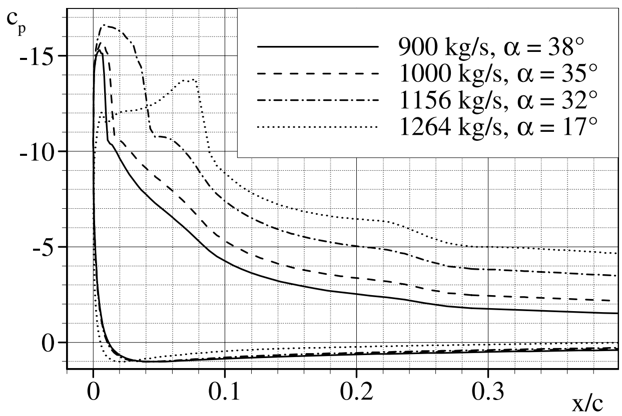

FIG. 3: Pressure distributions for different mass flow rates prior to separation onset, $\theta = 180°$, $Ma = 0.25$, $Re = 11.2\times10^6$.

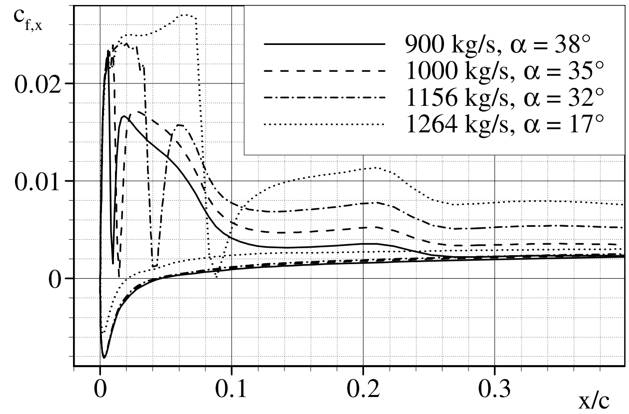

FIG. 4: Wall shear stress distributions for different mass flow rates prior to separation onset, $\theta = 180°$, $Ma = 0.25$, $Re = 11.2\times10^6$.

It becomes obvious that even at the smallest possible mass flow rate a subsonic flow in the inlet cannot be achieved. Nevertheless a similarity to subsonic pressure distributions becomes apparent since the supersonic region and thus the separation bubble move upstream with decreasing mass flow rate. Furthermore it is seen that the point of separation onset is shifted to higher angles of attack for a decreasing mass flow rate (1264 kg/s: $\alpha = 17.5°$, 1156 kg/s: $\alpha = 32.5°$,1000 kg/s: $\alpha = 35.5°$, 900 kg/s: $\alpha = 39.0°$).

In FIG. 5 a computed pressure distribution at the circumferential section $\theta = 180°$ is compared to the according measurement data for an angle of attack which features separation ($\alpha = 20.3°$). It can be seen that the solution is in good agreement with the measurement in regions of attached flow, namely on the outside of the nacelle. In the vicinity of separated flow ($x/c \approx 0.09$) in the inlet, however, the measured data is not well produced. This supports the authors' claim that an improved simulation methodology at the limits of the flight envelope is needed.

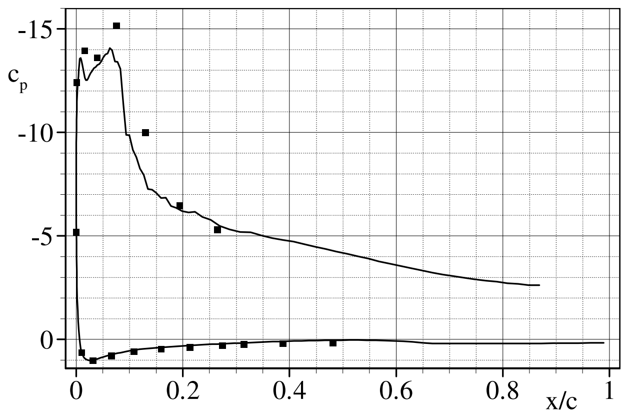

FIG. 5: Comparison between TAU simulation and measured data for the LARA nacelle, $\theta = 180°$, $Ma = 0.25$, $Re = 11.2\times10^6$, $\dot{m} = 1264\,\mathrm{kg/s}$, $\alpha = 20.3°$.

In the next step the dependency of the flow along the 180°-section on the geometry of the remaining circumferential sections was investigated. Therefore the $\theta = 180°$ section was rotated into an axisymmetric nacelle, once with a matching hilite area relative to the 3D nacelle and once with a matching fan area. The central body has been retained unchanged. FIG. 6 shows the resulting pressure distributions for $\dot{m} = 1156\,\mathrm{kg/s}$ and $\alpha = 32.0°$. It can be seen that the pressure distributions match best in places of identical cross-sectional areas. Thus it can be concluded that the distributions in the 180°-section at a constant mass flow rate depend solely on the cross-sectional area formed by the inlet and not on the exact geometries of the remaining circumferential sections. Thus the design of an axisymmetric flow-through nacelle is possible.

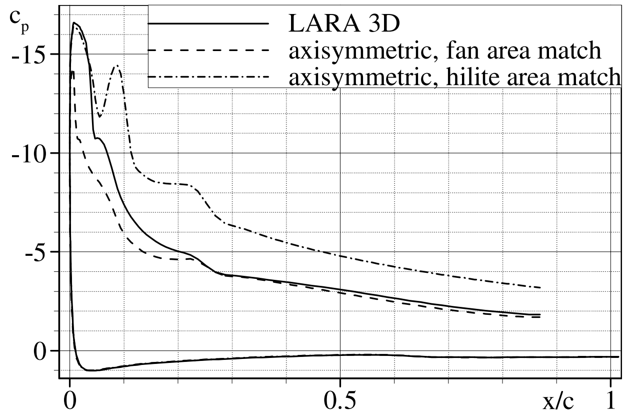

FIG. 6: Comparison between the 3D nacelle and axisymmetric nacelles with varying cross-sectional area, $\theta = 180°$, $Ma = 0.25$, $Re = 11.2\times10^6$, $\dot{m} = 1156\,\mathrm{kg/s}$, $\alpha = 32.0°$.

In FIG. 7 the influence of the central body is displayed. It is found that the pressure distributions are only affected in the aft part of the nacelle. The separation onset remains therefore unaffected which is why the flow-through nacelle can be designed without the need of a central body.

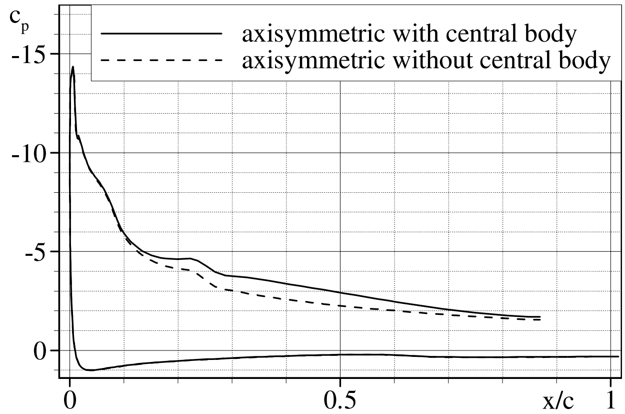

FIG. 7: Comparison between an axisymmetric nacelle with and without a central body, $\theta = 180°$, $Ma = 0.25$, $Re = 11.2\times10^6$, $\dot{m} = 1156\,\mathrm{kg/s}$, $\alpha = 32.0°$.

Furthermore a comparison between viscous and inviscid computations on the LARA nacelle yields that viscous and inviscid pressure distributions are in good agreement for attached flows (see FIG. 8). According to these results it is conceivable to design the flow-through nacelle with the help of inviscid computations up to the point of separation.

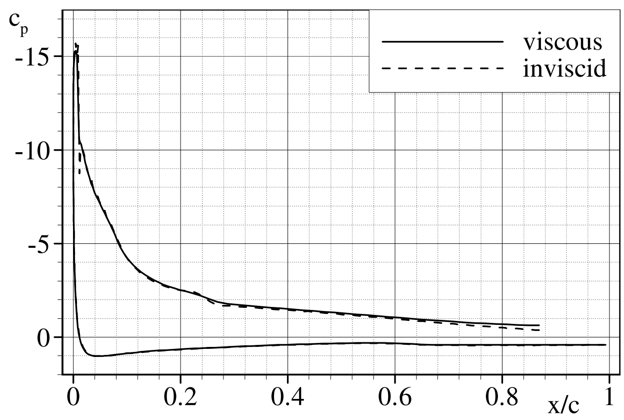

FIG. 8: Comparison between viscous and inviscid pressure distributions of the 3D nacelle, $\theta = 180°$, $Ma = 0.25$, $Re = 11.2 \times 10^6$, $\dot{m} = 900\,\mathrm{kg/s}$, $\alpha = 38.0°$.

As a final step the separation behaviour of the 3D LARA nacelle at wind milling conditions was investigated (see FIG. 9). It can be seen that the suction peak drops substantially with the loss of the high mass flow rates even though the free-stream velocity of $Ma = 0.25$ is kept constant. Furthermore FIG. 9 shows that the LARA nacelle now separates from the trailing edge at high angles of attack above 25 degrees without any inlet separation.

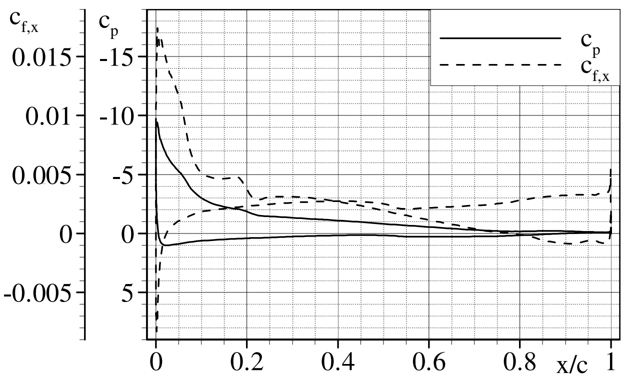

FIG. 9: Pressure and wall shear stress distributions of the LARA nacelle at wind milling conditions, $\theta = 180°$, $Ma = 0.25$, $Re = 11.2 \times 10^6$, $\alpha = 30.0°$.

4. FLOW-THROUGH NACELLE

4.1. Design Methodology

Based on the results in chapter 3.2 it was decided to design an axisymmetric flow-through nacelle without a central body. Only the circumferential section at θ=180° was altered using the design routine XFOIL[17], and viscous effects were not considered at this point. Afterwards the 180°-section was rotated into an axisymmetric nacelle, and viscous and inviscid 3D simulations were performed in TAU until the desired separation behaviour was achieved. Once again all viscous computations were undertaken assuming a fully turbulent boundary layer and employing the turbulence model Menter SST. The hybrid, unstructured grids were generated in Centaur [18], this time including 36 prism layers. The total number of points for each design case is about 2×10^6. In order to resemble the conditions during the prospective wind tunnel experiments all computations were performed at a free-stream velocity of $Ma = 0.15$ and at a maximum Reynolds number of $Re = 1.34 \times 10^6$.
As a starting point for the design a slightly modified geometry of the LARA nacelle's 180°-section was chosen (see FIG. 10). It equals the original LARA coordinates on the inside up to 22 % chord length and up to 65 % chord length on the outside. FIG. 11 shows a comparison of the LARA pressure distributions at $\theta = 180°$ for the 2D computation in XFOIL as well as for the viscous and inviscid simulations in TAU. At the depicted angle of attack $\alpha = 25.0°$ the flow is on the threshold to separation but still attached. Like the LARA nacelle at wind milling conditions the LARA geometry in FIG. 10 separates at angles of attack higher than 25 degrees and features a trailing edge separation without any inlet separation. Furthermore it can be seen in FIG. 11 that the viscous and inviscid distributions are still in quite good agreement even though the Reynolds number has been significantly reduced. There is a big difference between the 2D and 3D simulations to be observed, though. Much of the suction peak is lost during the step from a 2D airfoil design to a 3D nacelle design. Changes in the XFOIL design routine thus have to be oversized in order to produce a sufficient change in the final flow-through nacelle design.

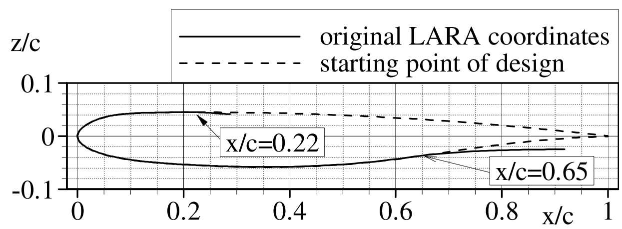

FIG. 10: Starting geometry in the section $\theta = 180°$ for the design, derived from the LARA nacelle.

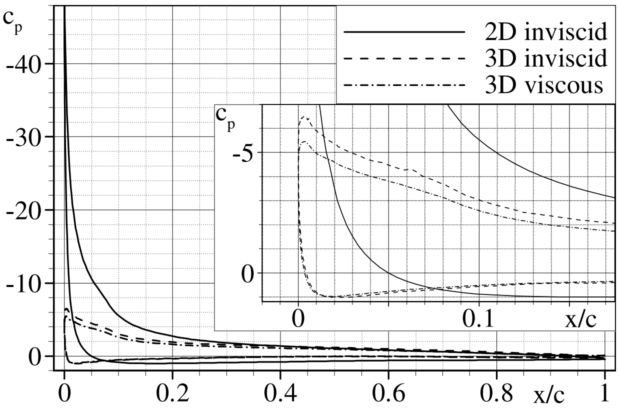

FIG. 11: Comparison between the pressure distributions of the starting geometry for the 2D and 3D computations, $\theta = 180°$, $Ma = 0.15$, $Re = 1.34 \times 10^6$, $\alpha = 25.0°$.

4.2. Design Results

The final design was achieved after several iterations in the design process and shows for $\alpha \geq 15°$ the typical take-off separation around the θ=180°-section (cf. FIG. 12 and 2). The designed contour is given in comparison to the starting geometry in FIG. 13. It can be seen that the design features a recess in its contour followed by a kind of bump. Both recess and bump are needed to control the growth of the separation bubble which will be explained in detail later. The bump causes a recovery in the flow which can be observed in the pressure and wall shear stress distributions in FIG. 14 and 15. The comparison of the 2D and 3D pressure distributions for the final design shows once again good agreement between viscous and inviscid 3D simulations in areas of attached flow. The maximum suction peak which could be achieved for the flow-through nacelle is $c_p = -2.4$. This is due to the low mass flow rate and the lower free-stream velocity of $Ma = 0.15$ in the wind tunnel. Nevertheless the design features the desired pressure-induced separation onset at $\alpha = 15°$ and $x/c = 0.125$ which resembles the original LARA reference case with $\dot{m} = 1264\,\mathrm{kg/s}$, $\alpha = 17.5°$, and $x/c = 0.09$.

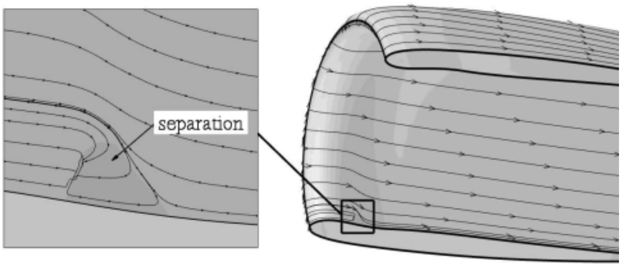

FIG. 12: Flow field of the designed flow-through nacelle at $Ma = 0.15$, $Re = 1.34 \times 10^6$, $\alpha = 15.0°$.

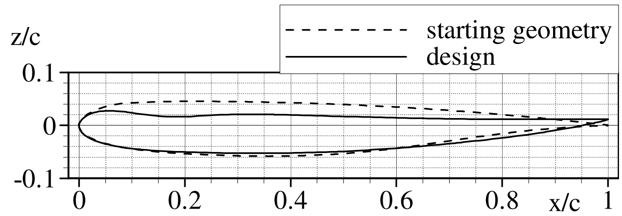

FIG. 13: Final design and starting geometry, $\theta = 180°$.

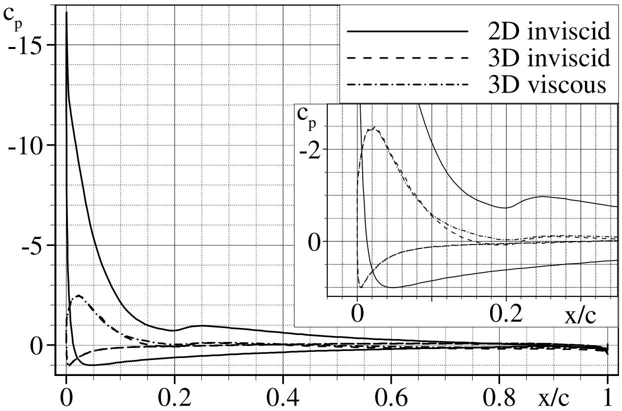

FIG. 14: Comparison between the design pressure distributions for 2D and 3D computations, $Ma = 0.15$, $Re = 1.34 \times 10^6$, $\alpha = 15.0°$.

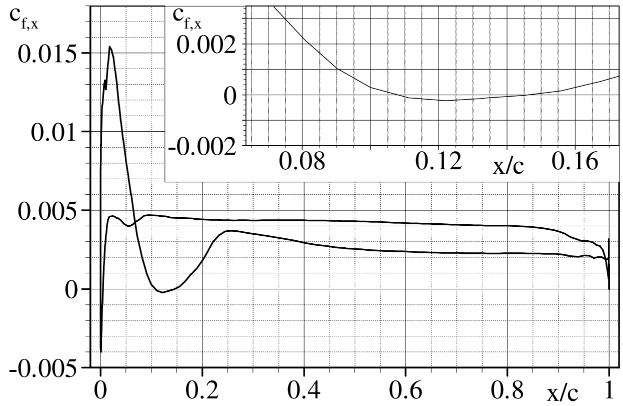

FIG. 15: Wall shear stress distribution of the final design, $Ma = 0.15$, $Re = 1.34 \times 10^6$, $\alpha = 15.0°$.

After achieving a satisfying nacelle design the dependency of the separation onset on the applied turbulence model was investigated. In FIG. 16 the wall shear stress distributions at $\alpha = 15°$ are plotted for the known Menter SST turbulence model as well as for the Spalart Allmaras (SA) and the Spalart Allmaras model with Edwards modification (SAE). While Menter SST shows already separated flow at $\alpha = 15°$, SA and SAE tend to separate later, namely at $\alpha = 17°$ and $\alpha = 19°$ respectively.

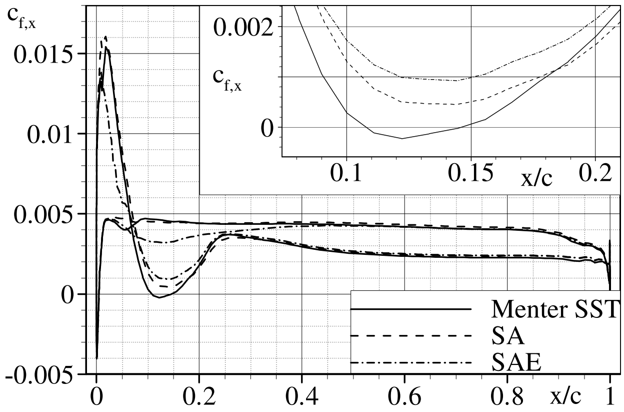

FIG. 16: Comparison between the shear stress distributions of computations with different turbulence models, $Ma = 0.15$, $Re = 1.34\times10^6$, $\alpha = 15.0°$.

Within the iterative design process it was found that the turbulent separation bubble tends to break up and spread out over the whole chord length very shortly after the separation onset. To avoid this bubble break-up a bump behind a recess is included in the contour of the 180°-section. The relative growth of the separation bubble for the final design and the LARA nacelle can be seen in FIG. 17. The point of separation onset is shifted to the graph's origin for a better comparison. The different turbulence models predict a maximum interval of five degrees for the rise in angle of attack before the separation bubble breaks up. Also the difference between the shock-induced separation of the LARA nacelle and the design's separation which is due to a continuous adverse pressure gradient can be observed.

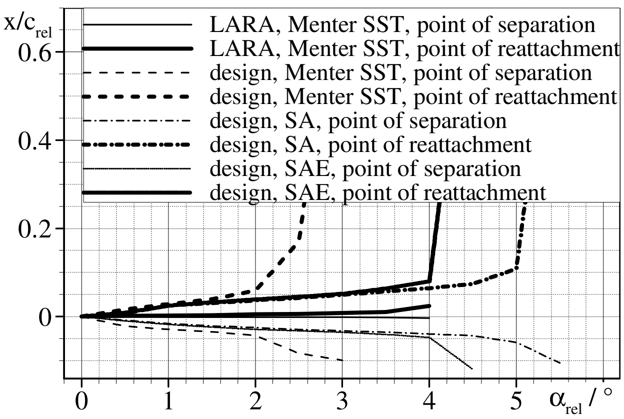

FIG. 17: Comparison between the growth of the separation bubble in streamwise direction for the design and LARA nacelle.

FIG. 18 depicts the growth of the separation bubble in circumferential direction and states that all computational models feature a similar inclination. The separated area never extends an angle of 40° between the edge of the separation bubble and the 180°-section of the nacelle. Furthermore it can be observed that the area of reversed flow is smaller than 1 mm in the wall-normal direction (see FIG. 19). Only about 1° before the bubble break-up the bubble gains in size normal to the wall. Thus prospective measurements will take place during this short interval with small changes in angle of attack of about 0.25°.

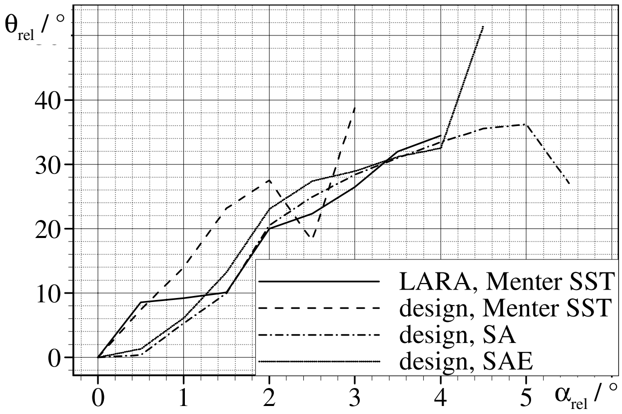

FIG. 18: Comparison between the growth of the separation bubble in circumferential direction for the design and LARA nacelle.

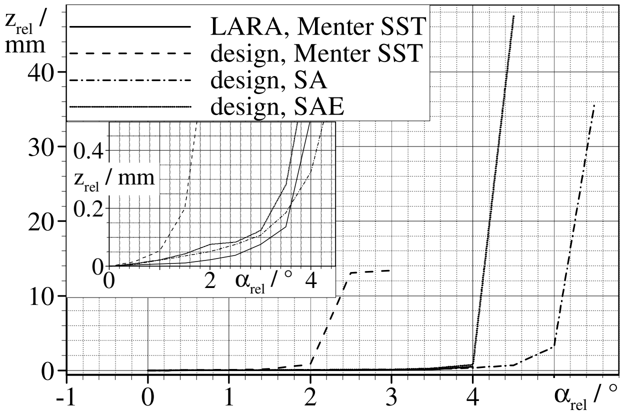

FIG. 19: Comparison between the growth of the separation bubble in wall normal direction for the design and LARA nacelle.

Finally the influence of the wind tunnel walls on the separation onset was investigated. The experiments are planned to take place in the low speed wind tunnel "MUB" at the Institute of Fluid Mechanics in Braunschweig which has a 1300 x 1300 mm^2 closed test section. The wind tunnel walls were simulated as inviscid walls. In FIG. 20 it can be seen that the appearance of the wind tunnel has little effect on the flow through the nacelle. The pressure distributions show no major discrepancies.

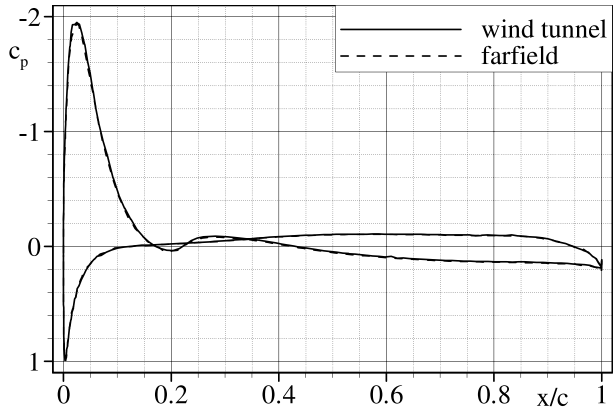

FIG. 20: Comparison between the pressure distributions with and without wind tunnel interference, $\theta = 180°$, $Ma = 0.15$, $Re = 1.34 \times 10^6$, $\alpha = 12.0°$.

4.3. Design Sensitivities

In the course of the design process special emphasis was put on the question which design parameters could effectively be used to control the separation onset and the value of the suction peak. In the following paragraphs these sensitivities will be presented based on the final design.

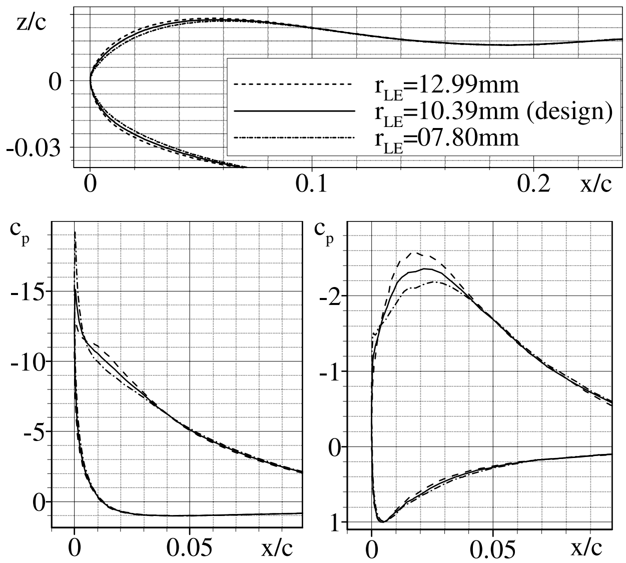

FIG. 21: Comparison between the 2D (left) and 3D (right) pressure distributions for different leading edge radii, $\theta = 180°$, $Ma = 0.15$, $Re = 1.34 \times 10^6$ (3D), $\alpha = 14.5°$.

In FIG. 21 the influence of the leading edge radius is investigated. The left hand side shows the different pressure distributions at $\theta = 180°$ for the inviscid 2D simulations in XFOIL. The right hand side depicts the according distributions for the viscous 3D nacelle computations with TAU. As expected the 2D distributions yield a rising suction peak for a decreasing leading edge radius. Regarding the nacelle simulations, however, an opposite behaviour can be observed, because the 3D inlet flow displays a shift of the pressure minimum towards the point of minimum inlet area at $x/c = 0.06$, in comparison to the 2D result. Then the smaller leading edge radius redistributes surface curvature away from the inlet suction peak and hence reduces the peak value. Thus an increased leading edge radius features here an earlier separation onset and vice versa.

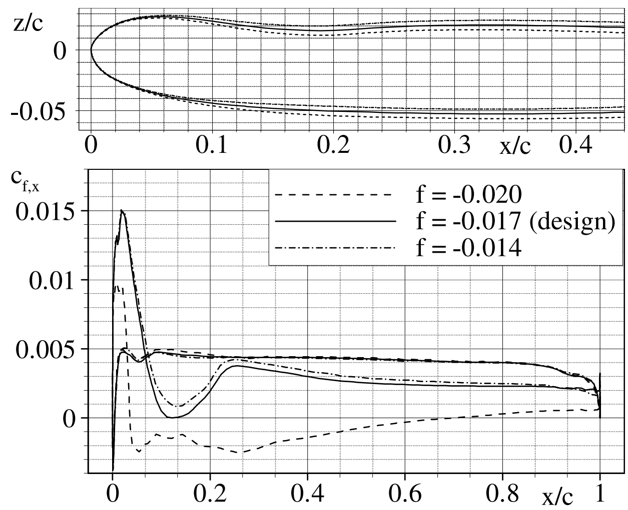

FIG. 22: Comparison between wall shear stress distributions of different camber, $\theta = 180°$, $Ma = 0.15$, $Re = 1.34 \times 10^6$, $\alpha = 14.5°$.

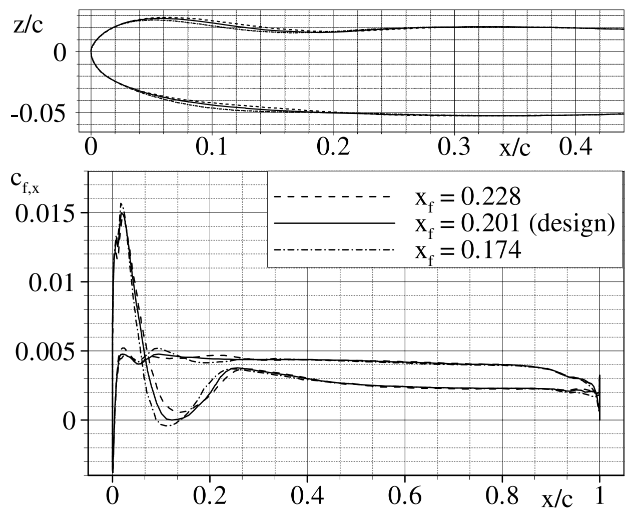

FIG. 23: Comparison between wall shear stress distributions for different positions of maximum camber, $\theta = 180°$, $Ma = 0.15$, $Re = 1.34 \times 10^6$, $\alpha = 14.5°$.

FIG. 22 shows the wall shear stress distributions at $\alpha = 14.5°$ for contours of varying camber. While separation onset occurs at smaller angles of attack for increased negative camber, the separation is delayed in cases of reduced camber. Looking at the investigations in FIG. 23 it can be observed that the position of maximum camber is another powerful parameter to control not only the angle of separation onset but also the chord-related position of the separation bubble. The more the maximum camber is shifted towards the leading edge, the closer to the leading edge the flow will separate. Also a shift to smaller angles of attack can be determined for the separation onset while moving x_f towards the leading edge. For the present design the strong effects of maximum camber and its position were used by introducing a distinct recess in the contour which can be seen in FIG. 13.

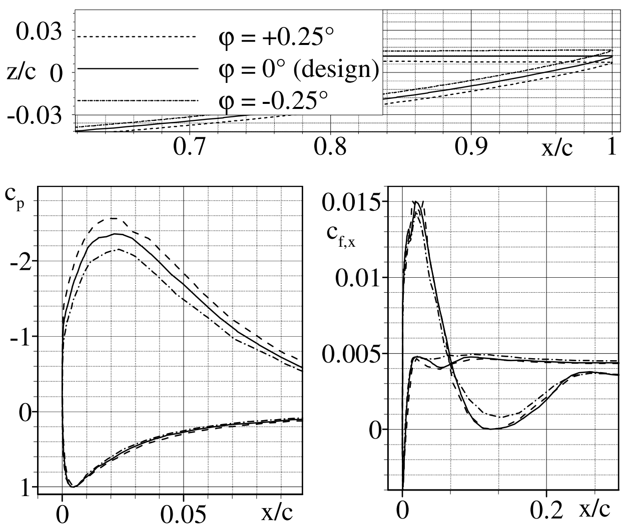

FIG. 24: Comparison between pressure (left) and wall shear stress distributions (right) for nacelles with different diffuser angles, $\theta = 180°$, $Ma = 0.15$, $Re = 1.34 \times 10^6$, $\alpha = 14.5°$.

As another parameter the influence of the so-called diffuser angle φ was analysed. A change in diffuser angle is achieved by rotating the 180°-section around its leading edge before it is rotated into an axisymmetric nacelle. The 2D simulations therefore show an increase in the suction peak with growing diffuser angle since nothing else but a larger angle of attack is produced. In the 3D case exactly the same behaviour can be extracted from the pressure distributions (see FIG. 24, left). Furthermore an increase in the cross-sectional area at the trailing edge beyond the design does not seem to alter the onset of separation significantly while a reduced diffuser angle causes the nacelle to separate at higher angles of attack (see FIG. 24, right). In the course of the design process it was found, though, that a rise in diffuser angle is usually accompanied by an increase in suction peak and an earlier separation onset. Therefore the increased diffuser angle in FIG. 24 is no advantage compared to the design since the recovering effect of the bump is impaired by the rotation around the leading edge.

The importance of the bump in the contour of the 180°-section is once more shown in FIG. 25. At an angle of attack of $\alpha = 17.0°$ the design is still capable of producing a distinct separation bubble. The contour without the bump on the other hand shows separation across almost the whole chord length. Thus the bump is a necessary means to create a recovery in the flow which keeps the separation bubble from breaking up over a certain increase in angle of attack.

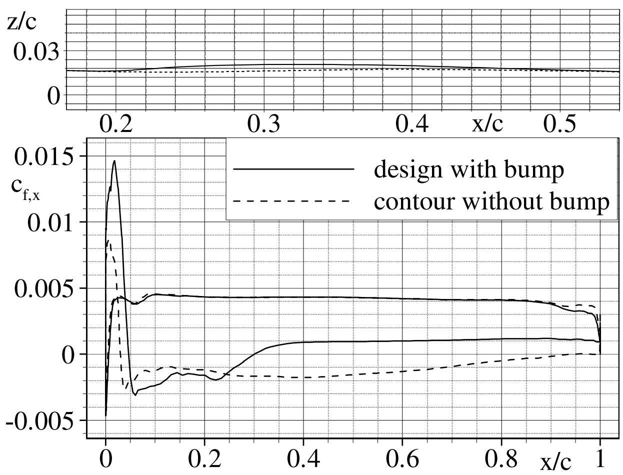

FIG. 25: Comparison between wall shear stress distributions for nacelles with and without a recovery bump, $\theta = 180°$, $Ma = 0.15$, $Re = 1.34 \times 10^6$, $\alpha = 17.0°$.

5. CONCLUSION

Steady-state RANS computations were carried out for the so-called LARA nacelle as an example for a powered inlet at take-off conditions. The 3D nacelle was found to separate solely on the intake inner bottom lip for a range of mass flow rates between 900 kg/s and 1264 kg/s. A comparison of the simulations to measured pressure distributions showed good agreement in areas of attached flow but uncertainties around separated flow regions. For the design of a flow-through nacelle with a similar boundary layer loading under wind tunnel conditions a nacelle of rotational symmetry and without a central body was found to be sufficient. Furthermore it was shown that inviscid calculations are acceptable for the design process up to the point of separation onset. Finally, a sophisticated design could be achieved which features the desired separation behaviour of powered inlets. Also a variety of geometrical parameters were identified which can effectively be used to control separation onset and the suction peak. Simulations of the wind tunnel walls were found to have no influence on the separation onset. The present design will serve as a test bed for detailed flow measurements in the future.

6. ACKNOWLEDGEMENTS

The authors would like to thank Dr. Hepperle from the DLR Braunschweig for providing all data concerning the LARA nacelle as well as Mr. Probst from the TU Braunschweig for making Gridgen grids of the LARA nacelle available. This work is part of the coordinated German research project “Simulation des Ueberziehens von Tragfluegeln und Triebwerksgondeln” and is funded by the German Research Foundation, DFG.

7. REFERENCES

[1] Inlets and nozzles for aerospace engines. AGARD CP No. 91, 1971.

[2] Engine response to distorted inflow conditions. AGARD CP No. 400, 1986.

[3] Goldsmith, E.L., Seddon, J.: Practical intake aerodynamic design. AIAA Edu. Series, 2nd Ed., 1999.

[4] Willmer, A.C., Brown, T.W., Goldsmith, E.L.: Effects of intake geometry on circular pitot intake performance at zero and low forward speeds. AGARD CP No. 301, 1981.

[5] Quémard, C., Garçon, F., Raynal, J.-C.: High Reynolds number air intake tests in ONERA F1 and S1Ma wind-tunnels. In: H. Hoheisel (Ed.): “Aspects of Engine-Airframe Integration for Transport Aircraft”, Proceedings of DLR Workshop, DLR Mitt. 96-01, 1996.

[6] Prasad, A.K.: Stereoscopic particle image velocimetry. Exp. Fluids 29, pp. 103-116, 2000.

[7] Lindken, R., Di Silvestro, F., Westerweel, J., Nieuwstadt, F.T.M.: Turbulence measurements with μ-PIV in large-scale pipe flows. In: Proceedings of the 11th International Symposium on Application of Laser Technology to Fluid Mechanics, Lisbon, Portugal, 8-11 July, 2002.

[8] Kähler, C.J., Scholz, U., Ortmanns, J.: Wall-shear-stress and near-wall turbulence measurements up to single pixel resolution by means of long-distance micro-PIV. Exp. Fluids 41, pp. 327-341, 2006.

[9] Elsinga, G., Scarano, F., Wieneke, B., Oudheusden, B.: Tomographic Particle Image Velocimetry. Exp. Fluids 41, pp. 933-947, 2006.

[10] Hain, R., Kähler, C.J., Michaelis, D.: Tomographic and time resolved PIV measurements on a finite cylinder mounted on a flat plate. 7th International Symposium on Particle Image Velocimetry, Rome, Italy, 11-14 September, 2007.

[11] Hain, R., Kähler, C.J.: Fundamentals of Multiframe Particle Image Velocimetry (PIV). Exp. Fluids 42, pp. 575-587, 2007

[12] Mullender et al.: Hybrid laminar flow nacelle design. 20th Congress of the International Council of the Aeronautical Sciences, Sorrento, Napoli, Italy, 8-13 September, 1996.

[13] Gerhold, T.: Overview of the hybrid RANS code TAU. Notes on Numerical Fluid Mechanics and Multidisciplinary Design, Volume 89, pp. 81-92, 2005.

[14] Deutsches Zentrum fuer Luft- und Raumfahrt: TAU-Code User Guide. Release 2006.1.0, DLR, April, 2006.

[15] Gridgen: http://www.pointwise.com, July, 2007.

[16] ONERA: LARA laminar flow nacelle off-design performance tests in the ONERA F1 wind tunnel. Study No. 4365 AY 178 G, July, 1994.

[17] Drela, M.: XFOIL: An analysis and design system for low Reynolds number airfoils. In Mueller, T.J. (Ed.): Low Reynolds number aerodynamics. Springer, Lecture notes in engineering, pp. 1-12, 1989.

[18] Centaur: http://www.centaursoft.com, July, 2007.